Agricultural and Forest Meteorology 244–245 (2017) 136–150

Contents lists available at ScienceDirect

Agricultural and Forest Meteorology

journal homepage: www.elsevier.com/locate/agrformet

Observations of microscale internal gravity waves in very stable atmospheric boundary layers over an orchard canopy

Shane D. Mayor*

California State University, Chico, Chico, CA 95928, USA

ARTICLE INFO

Keywords:
Gravity waves
Internal waves
Wave breaking
Shear flow instabilities
Stable boundary layers
Turbulence
Canopy
Lidar
Aerosol

ABSTRACT

Fifty-three episodes of internal gravity waves, with horizontal wavelengths ranging from 30 to 100 m, were identified in time-lapse animations of numerically filtered elastic backscatter lidar images collected during the Canopy Horizontal Array Turbulence Study (CHATS). The waves existed in and above a 10 m tall walnut orchard and are also present in time-series data of meteorological variables such as wind and temperature as measured by in situ sensors at multiple heights on a 30 m tower centrally located in the lidar scan area and inside the $(1.6\ km)^2$ orchard. All of the episodes occurred at night in the presence of temperature inversions and light winds. Wave periods from time-series analysis of the in situ data range from 20 to 100 s. Sequences of lidar images reveal that the waves propagate in the direction of and at phase speeds less than that of the mean wind. The in situ data indicate the presence of a wind shear maximum and an inflection point at the top of the canopy. Gradient Richardson numbers near that altitude range between 0 and 0.20 indicating hydrodynamic instability. Range versus height lidar images from one case show the wave structures tilting downstream with altitude. In some cases, horizontal scans reveal that the gradient of aerosol backscatter tends to be larger on the upwind side of the crests. The environment and observations are consistent with the prevailing theory that the waves are the result of inflection point instability and the lidar data suggest that in 42% of the episodes the waves may have begun, or be on the verge of, breaking.

1. Introduction

Temperature inversions routinely form during the night over land when the surface of the earth cools faster than the air above it. Such environments are statically stable arrangements of the lowest levels of the atmosphere that resist the production of turbulence and support vertical oscillations known as internal gravity waves (Fernando and Weil, 2010; Sutherland, 2010; Nappo, 2012; Mahrt, 2014). Herein, observations of organized groups of relatively *clean*[1] internal gravity waves in the very stable, nocturnal atmospheric boundary layer over a $(1.6\ km)^2$ walnut orchard block in the Central Valley of California are presented. The dataset is unique because of the simultaneous availability of wind velocity and air temperature measurements from mast-mounted fast-response in situ sensors in the form of time-series at multiple altitudes and 2D images of relative aerosol backscatter from a ground-based scanning elastic lidar system. The use of both types of data begin to reveal the 3D structure and motion of waves in the atmospheric roughness sublayer. The waves are significant because continued amplification will eventually result in unstable vertical arrangements of the air that lead to *breaking* and episodes of turbulence that are responsible for vertical fluxes of heat, momentum, and trace gases (Fitzjarrald and Moore, 1990; Sun and Coauthors, 2015).

Waves over forest canopies are commonly referred to as *canopy waves* because they result from the shear-induced inflection point instability (Kundu et al., 2016) that the canopy induces on the mean horizontal flow. Prior studies of canopy waves include those by Paw U et al. (1992), Raupach et al. (1996), Lee et al. (1996), Lee (1997), Lee et al. (1997), Lee and Barr (1998), Pulido and Chimonas (2001), Hu et al. (2002), Finnigan et al. (2009), Gavrilov et al. (2011), and Belcher et al. (2012). Very recent work includes Arnqvist et al. (2016) and Bailey and Stoll (2016). The waves described herein likely correspond to the waves shown in panels a and b of Fig. 14 in Finnigan et al. (2009). That is, most of them appear to have an approximately sinusoidal shape in the direction of the mean flow such as shown in Fig. 14a in Finnigan et al. (2009) and about 42% of the cases exhibit asymmetry that is a characteristic of Kelvin-Helmholtz billows such as shown in Fig. 14b in Finnigan et al. (2009). These phases of wave development occur prior to the more developed turbulence that makes it difficult to

* Corresponding author at: California State University, Chico, 400 West First Street, Chico, CA 95928, USA.
E-mail address: sdmayor@csuchico.edu.

[1] Clean refers to waves with a number of cycles of approximately constant amplitude and period.

http://dx.doi.org/10.1016/j.agrformet.2017.05.014
Received 2 December 2016; Received in revised form 8 April 2017; Accepted 18 May 2017
Available online 15 June 2017

recognize the turbulent coherent structures that occur after the waves break as shown in Figs. 14c and 14d in Finnigan et al. (2009). However, there is one important difference: the waves herein exist in stably stratified environments whereas the work described by Finnigan et al. (2009) is focused on neutral conditions. An excellent summary of instabilities in stratified shear flows can be found in Lawrence et al. (2013). Papers treating the details of internal wave mechanics include Carpenter et al. (2013). Reviews of coherent eddy structure over plant canopies can be found in Shaw et al. (2013) and Patton and Finnigan (2013).

This paper is organized as follows. Section 2 describes the lidar system that provided the 2D cross-sectional images of the waves. Section 3 presents the experimental design. Section 4 explains why the lidar is capable of observing the waves. Section 5 describes the data analysis methods. Section 6 describes four episodes in depth. Section 7 describes the mean environmental conditions and wave characteristics of all 53 episodes. Section 8 presents the conclusions. The primary goals of the paper are to (1) document the experimental methods used to observe the waves (in particular, use of elastic backscatter aerosol lidar) and (2) describe the physical characteristics of the observed waves. It is hoped that the former will facilitate improved observations of canopy waves in future field experiments and the latter will aid the understanding of the transition of flows to turbulence in stably stratified forest environments.

2. REAL

The Raman-shifted Eye-safe Aerosol Lidar (REAL) (Mayor and Spuler, 2004; Spuler and Mayor, 2005; Mayor et al., 2007) is a ground-based, scanning elastic backscatter lidar. It does not have the ability to sense the wind-induced frequency shift of the backscattered laser radiation as Doppler lidars do. The strength of the REAL is in its ability to provide high-resolution images of elastic backscatter intensity. This is accomplished by using short and energetic laser pulses, sensitive analog direct detection, and 40-cm diameter receiving optics. Operation at the infrared wavelength of 1.54-μm results in an invisible beam and strong pulse energy while remaining eye-safe. Specifications of the lidar system as configured for the experiment reported herein are listed in Table 1 of Mayor et al. (2012).

The REAL operates at 10 Hz pulse repetition frequency and each laser pulse is sufficiently energetic that useful backscatter intensity signal can be detected to several kilometers range from individual pulses. No averaging of the backscatter from multiple pulses is necessary as is the case with micropulse lidars (Spinhirne, 1993; Mayor et al., 2016). The data acquisition system samples the backscatter at 100-million samples per second (MSPS) resulting in one data point every 1.5 m in range. The REAL data, like all scanning radar and lidar data, are collected in a spherical coordinate system with coordinates of elevation, azimuth, and range. As a result, the density of data points that makes up a scan decrease with range. The REAL, like many lidars, uses a beam steering unit (BSU, also known as a *scanner*) to collect either nearly-horizontal or vertical atmospheric cross-sections referred to as *scans*. The nearly-horizontal scans are known as *plan position indicator* or PPI scans and the vertical scans are known as *range height indicator* or RHI scans. The transmitted laser pulses are approximately 7 cm diameter as they exit the scanner and increase to about 0.5 m diameter at 1.61 km range.

3. Experimental design

Deployment of the REAL was an appendix to the Canopy Horizontal Array Turbulence Study (CHATS) (Patton and Coauthors, 2011; Dupont and Patton, 2012a,b). The deployment was a pilot study aimed at determining whether the lidar could detect *turbulent* coherent structures—not waves and billows in strongly stably stratified conditions as described herein. The main focus of CHATS was the operation of height-adjustable horizontal arrays of sonic anemometers deployed in the orchard. In addition, a 30-m tall instrumented tower (the Integrated Surface Flux Facility, ISFF) was deployed nearby in the orchard to provide vertical profiles of meteorological variables. The REAL was located 1.61 km north of the 30-m tall tower (see Fig. 1). From this distance, the lowest elevation angle for a PPI scan that could observe the atmosphere over the orchard was about 0.2° above horizontal. However, the REAL platform was precisely positioned in the east-west direction so that the RHI scans would fall between a pair of rows of trees adjacent to the ISFF. In this way, RHI scans could sample the atmosphere below the canopy top when the narrow region between the rows of trees was clear of foliage.

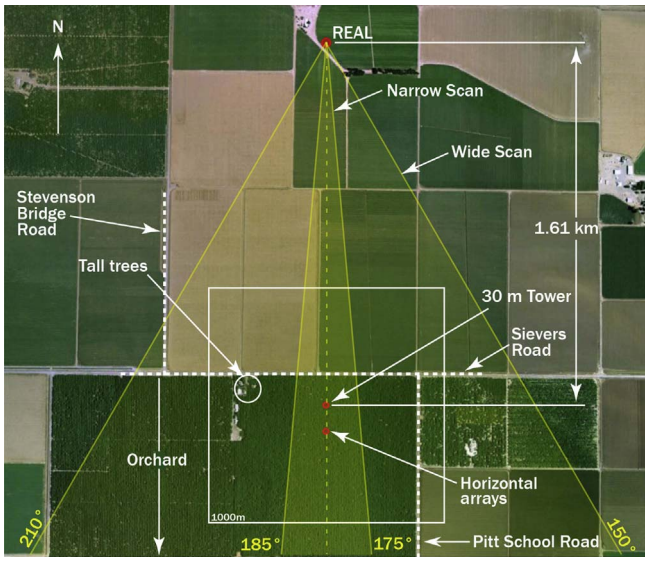

Fig. 1. Plan view of the experimental area for the 2007 CHATS experiment. The REAL was located 1.61 km directly north of the 30-m-tall NCAR ISFF tower. The analysis of waves was limited to the 1 km^2 square centered on the tower (outlined in white). Wide and narrow PPI sector scan regions from the REAL are shaded in yellow. The orchard was south of Sievers Road which is indicated by a horizontal dashed white line. (For interpretation of the references to color in this figure legend, the reader is referred to the web version of this article.)

The 10 Hz laser pulse rate of the REAL is not adjustable, but the angular speed at which the scanner moves its mirrors is fully adjustable. For CHATS, and subsequent experiments, experience shows that it works best to scan at 4° s^{-1} in order to observe areas spanning several square kilometers and complete the sector scans[2] within 30 s. This scan rate provides sufficient temporal coherence of turbulent aerosol features in time-lapse animations of PPI scans to estimate wind vectors objectively (Mayor et al., 2012). It is also convenient, if not intentional, that the spacing between the radial arrays at 1.61 km range is about 10 m—and a good match for Cartesian grids with the same grid spacing which is necessary for application of motion estimation algorithms. However, identification of the wave episodes was based on visual inspection of filtered backscatter data rendered to images at 1.5 m range increments. The high range resolution of the REAL, and images rendered in the native polar coordinate system, improves one's ability to identify these very fine scale waves.

Determining the true elevation angle of the lidar beam is important in order to link the aerosol features in the lidar images with the in situ data from the closest corresponding altitude on the tower. The location of the tower in the PPI images can be easily determined by the occasional hard target reflections that it causes. The hard target reflections from the tower, however, are intermittent in time-lapse animations of PPI scans because the laser pulses in one scan are not usually projected

[2] A 60° sector scan with useful data from 500 m to 3 km range covers 4.6 square kilometers.

at the same azimuth angles in subsequent scans. For example, in one scan, a laser pulse may strike a guy wire and on a subsequent scan, the pulses may pass through the regions between the guy wires and the central column of the tower.

The pointing azimuth and elevation of the REAL were initially calibrated by blocking the lidar's photodetector and executing a computer program that directs the BSU to track the sun. The position of the sun in the sky can be determined accurately and precisely based on position, date, and time, and the sun can be considered a distance point source of radiation that results in parallel visible rays streaming into the lidar receiver subsystem. Staff can adjust constants in the BSU sun tracking program until they observe rays from the sun focused on the entrance aperture to the blocked photodetector throughout an entire day. This procedure was performed only at the beginning of the CHATS experiment. Unfortunately, the subsequent trenching and flooding of a nearby agricultural irrigation ditch placed one side of the lidar platform (a trailer with two shipping containers) periodically on wet soil while the other side remained on dry, firm ground. Because the instrument was remotely operated from Boulder, Colorado during most of the experiment, staff were not always on site to know that conditions had changed. Staff from NCAR periodically visited the REAL site, and on at least one occasion attempted to level the platform. However, the attitude of the trailer was not measured and therefore the elevation angles recorded in the lidar data files are only as accurate as the position of the trailer was relative to its initial position. Tipping the trailer by 1 mm on one side results in a change of the lidar beam at the range of the ISFF tower (1.61 km) by 0.5 m altitude.

In addition, the vertical gradient of air density has a small effect on the trajectory of horizontally aimed laser pulses. This is due to the vertical gradient in the optical refractive index. During neutral stability conditions (i.e., the environmental lapse rate equals the dry adiabatic lapse rate of $0.0098^{\circ}\mathrm{C\,m^{-1}}$), the atmosphere *bends* the lidar pulse's propagation path down by about 3 cm over the first 1.61 km. In very stable environments, like those supporting the canopy waves, the effect is stronger. For an average lapse rate of about $-0.10^{\circ}\mathrm{C\,m^{-1}}$, typical of the conditions when the canopy waves were present, the propagation path would be bent down by about 17 cm in the first 1.61 km. The strongest temperature inversions[3] during the canopy wave episodes (about $-0.26^{\circ}\mathrm{C\,m^{-1}}$) resulted in a downward deflection of about 37 cm over the first 1.61 km. That amount of deflection is larger than the curvature of the earth (about 20 cm per 1.61 km). Therefore, the influence of the vertical structure of the atmosphere on the altitude of the lidar beam is small, but it does contribute to the uncertainty and perhaps the large number of hard target reflections from tree-top foliage that are observed in some of the PPI scans. (Please see Appendix A for a description of how the deflections were calculated.)

As a result of the above issues, the altitude of the lidar beam at the location of the ISFF tower was the largest uncertainty of the REAL data set from CHATS. It is estimated, based on the lateral span of the reflections from the tower guy wires, that the majority of the PPI scans collected during CHATS were between 18 and 20 m altitude at the range of the ISFF tower. However, at times during the experiment, the scans were much closer to the top of the canopy as evidenced by hard target returns from the highest tree branches and leaves protruding into the scan. Fig. 2 of Mayor et al. (2012) depicts a vertical cross section of the ISFF tower and canopy and the altitudes of the in situ sensors and laser pulses for a typical PPI scan at that range.

The deployment of REAL at CHATS took place between 15 March through 11 June 2007 and resulted in more than 275,000 PPI and 150,000 RHI scans from over 1850 h (77 days) of nearly continuous operation.[4] A variety of lidar scan strategies were conducted during the experiment. Since the primary goal was to observe fine-scale turbulent coherent structures over the orchard, the lidar was often programmed to make narrow (10°) RHI and PPI scans directly over the orchard. However, because ideal conditions for the in situ component of the experiment occurred only when the wind was from the south, wide-angle (45–60°) RHI and PPI scans were collected at other times. In many cases, RHI and PPI scans were collected in a continuously alternating fashion so that time-lapse animations of both horizontal and vertical atmospheric structure could be obtained simultaneously. In addition to scanning, the beam was periodically pointed toward a position near the tower and held stationary for a period of a few minutes to record fixed-beam data. Overall, the data set is unprecedented, but changing scan strategies, and the slight uncertainty in the altitude of the beam, complicate and limit the analysis.

4. Theory of aerosol lidar detection of canopy waves

The detection of canopy waves by the REAL was an unexpected result of CHATS. Indeed, a very first consideration was that the parallel bands in the images were an artifact induced by the instrument or data processing and not the result of real fluid waves. The possibility that the aerosol features were organized elsewhere and advected into the lidar's field of regard was also considered. However, by inspecting the in situ data from the ISFF, it became clear that the waves were real and a direct result of the local dynamics. This evidence is presented in Section 6.

Why is the REAL capable of detecting canopy waves? The current hypothesis is as follows: prior to sunset, during the usual sunny, fair-weather conditions of this location, the static stability is close to neutral and particulate matter is easily diffused in the lowest 30 m of the atmosphere (the range of altitudes sampled by the ISFF and REAL) by turbulence. The sources of particulate matter detectable by the lidar for this environment are numerous. They range from agricultural activities in the orchard in which the ISFF tower is installed, to similar activities from neighboring orchards and fields, to emissions from the nearby town of Dixon and Interstate Highway 80 (3 km to the south). Common events, such as trucks and tractors driving through the orchard (on a typical dry day) result in very significant plumes of dust (and perhaps engine exhaust) observable by the lidar at altitudes where the lidar was routinely probing (about 10 m above the 10-m tall canopy). Almost any orchard maintenance operation generates copious amounts of particulate matter. In addition, the trees themselves are a source of particulate matter especially when blossoming (presumably pollen) and the wind is sufficiently strong to raise the pollen or dust from the foliage.

As sunset approaches, the earth's surface cools faster than the air above it, resulting in a temperature inversion that forms from the ground up. Agricultural activity often occurs into the evening twilight hours. The slow deepening of the nocturnal inversion traps particulate matter into strata. Different sources of particulate matter for a given altitude could lead to varying aerosol properties such as particle type, concentration, or size distribution, and optical scattering characteristics. Similarly, the atmospheric water vapor concentration may take on a layered structure. Finally, as the lower layers become colder before the upper layers, they tend to have the highest relative humidities. Aerosol particles respond to the environmental relative humidity with hygroscopic particles swelling (Pahlow and Coauthors, 2006). As a result of these processes, vertical gradients of aerosol backscatter in the nocturnal surface layer over the orchard are found. Fig. 2A is an artist's rendition of this situation.

As the night progresses, the stable stratification strengthens resulting in frictional decoupling and the possibility of significant vertical wind shear over relatively small (i.e., 10 m) distances. The shear can induce wave motion as shown in Fig. 7.1.3 of Batchelor (1967). The aerosol field is then displaced vertically by the shear-induced internal gravity waves. The aerosol distribution that was horizontally invariant prior to wave activity becomes corrugated and volumes of air that cause high backscatter intensity are lifted by rising air and low backscatter

[3] Based on temperature profiles that resulted from 5-min averages. Much stronger temperature gradients are possible in the instantaneous profiles.

[4] All of the images from the experiment, resulting time-lapse animations, and details of all 53 episodes of canopy waves can be found in Supplementary material.

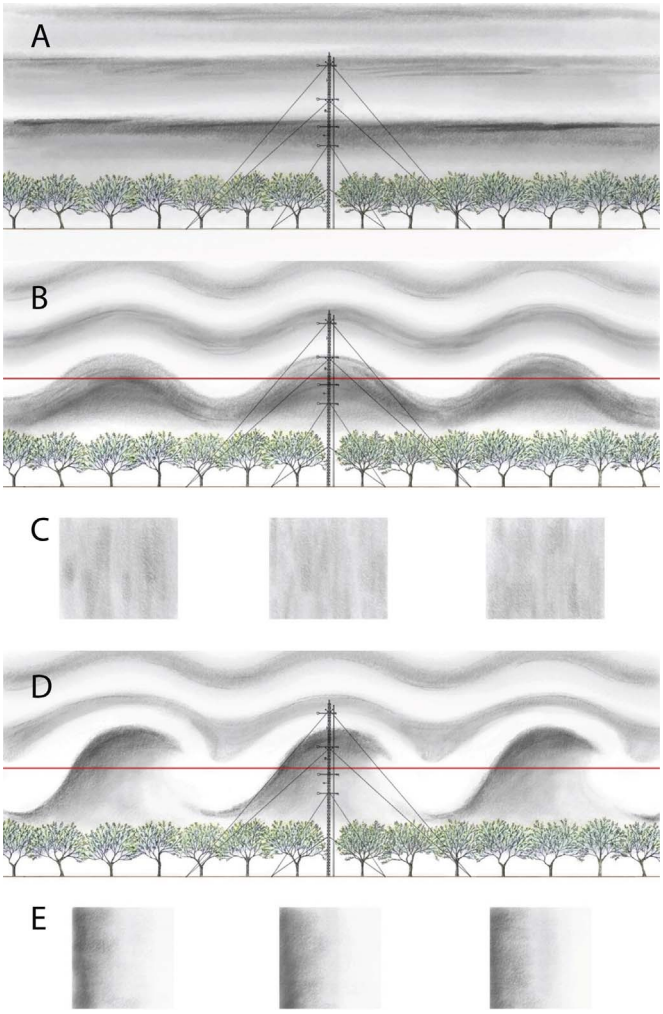

Fig. 2. Artist's rendition of aerosol scattering in vertical and horizontal cross sections of the lower atmosphere that explain why an elastic backscatter lidar may be capable of detecting canopy waves and the asymmetric structure of wave crests that is observable when wave breaking has started, or is about to start. Panel A corresponds to the early evening hours prior to the onset of waves. Panel B shows sinusoidal waves. Panel C shows homogeneous bands that would result from a horizontal scan at the altitude of the red line in Panel B. Panel D shows the most advanced stage of wave development where the wave crests have started, or are on the verge of, breaking. Panel E shows the asymmetric bands that would result from a horizontal scan at the altitude of the red line in Panel D. (For interpretation of the references to color in this figure legend, the reader is referred to the web version of this article.)

intensity is moved down by sinking air in the wave train. Fig. 2B is an artist's rendition of this state. The nearly-horizontally scanning lidar beam will propagate through raised and lowered regions of the displaced aerosol field resulting in a periodic backscatter field in which each wave crest is homogeneous in scattering intensity (Fig. 2C). Therefore, the lidar can reveal the wave activity through the aerosol field. If the waves continue to amplify, their structure becomes asymmetric as shown in Fig. 2D and 2E. That is, the more laminar flow on the upwind side of the wave crest preserves a strong gradient of aerosol backscatter as the beam traverses horizontally from the trough to the crest. However, as the beam traverses from the crest to the trough, turbulence associated with wave breaking increases the diffusion of the aerosol and the lidar images reveal a smaller gradient of backscatter in the region that is under and slightly downstream of the crest. This is illustrated clearly in Fig. 8.2.i and 8.3.i of Scorer (1997).

In practice, pulse to pulse variations in transmitted laser energy (and our inability to measure the energy with sufficient precision and normalize backscatter data accordingly) result in such strong variations in backscatter intensity that high-pass numerical filtering must be applied to the range-corrected backscatter intensity data in order to see the waves as shown in Fig. 3. The numerical filtering used is high pass median filtering and it is applied in the radial coordinate direction of the polar lidar data. For this work, and for work with motion estimation algorithms (Dérian et al., 2015; Hamada et al., 2016), a 333-point window resulting in the removal of features that are larger than 250 m in the radial direction was applied. If the proposed hypothesis is correct, the oscillations in backscatter intensity should be in phase with the position of air parcels, and therefore 90° out of phase from the vertical velocity.

The lidar images are uniquely capable of revealing the spatial structure and, when the frame rate is high enough, the propagation velocity of the waves. Some PPI images show what appear to be mergers of the wave crests and may be observational confirmation of what Thorpe (2002) refers to as *knots*. The weakness of the lidar data is the lack of backscatter intensity calibration. It is not possible to assign physical units to the backscatter intensity. For this reason, the color bars on the lidar images shown herein are labeled “relative backscatter intensity (dB)”. Subsequent experiments in Chico, California where the REAL laser beam was held stationary near an in situ particle counter indicate that, over short periods of time when the aerosol microphysical characteristics (such as normalized particle size distribution, particle type, etc.) are stationary, the relative backscatter intensity is most strongly correlated with particle concentration (Held et al., 2012).

Given a single PPI scan, the wavelength and the orientation of the wave crests can be determined through visual inspection. Given two consecutive PPI scans, the horizontal displacement of a given wavecrest can be measured if the time between scans is sufficiently small. Dividing the displacement by the time between PPI scans results in phase speed. The phase propagation direction was determined by drawing a line normal to the crests and measuring the angle of the normal line. With phase speed (v_p) and wavelength (λ), the period (τ) of the waves can be calculated through the relationship $\tau = \lambda / v_p$. Hence, using only lidar data, wave period as would be observed from a stationary point in space can be identified and compared with values determined exclusively from time-series analysis of velocity and thermodynamic data from tower-mounted in situ sensors.

5. Data analysis methodology

The time-lapse animations of the nearly-horizontal PPI scans were carefully examined for the presence of fine-scale wave packets (Jachens and Mayor, 2012). More precisely, a human watched time-lapse animations of all the high-pass median filtered PPI scans from CHATS and noted when waves were apparent at the ISFF tower location. A wave packet is distinct from other aerosol features observed in the lidar images in that the linear bands of enhanced backscatter intensity tend to be oriented perpendicular to the wind direction and the phase propagation direction. Furthermore, they appear to have a high degree of spatial and temporal coherence compared to plumes and wind parallel streaks sometimes observed during periods of turbulent flow. For a wave packet to be included as an episode in this study, it must have passed through the location of the ISFF tower and existed longer than one minute. Subjective judgments of the coherence of the wave packets were based on the clear identification of crests and troughs and movement together as a group. Following these requirements, 52 wave episodes were identified from the 3-month data set. Episodes range in time from a few minutes to more than 1 h in duration. A fifty-third case was identified from the careful inspection of RHI scans.

To focus the analyses and extract the salient features of the environment supporting the wave activity, a 5-min period of time per episode corresponding to when the waves appeared most pronounced in the lidar imagery was chosen. Those lidar images were carefully examined to determine wavelength and wave crest orientation. The extraction of quantitative wave properties was done by projecting the 1-

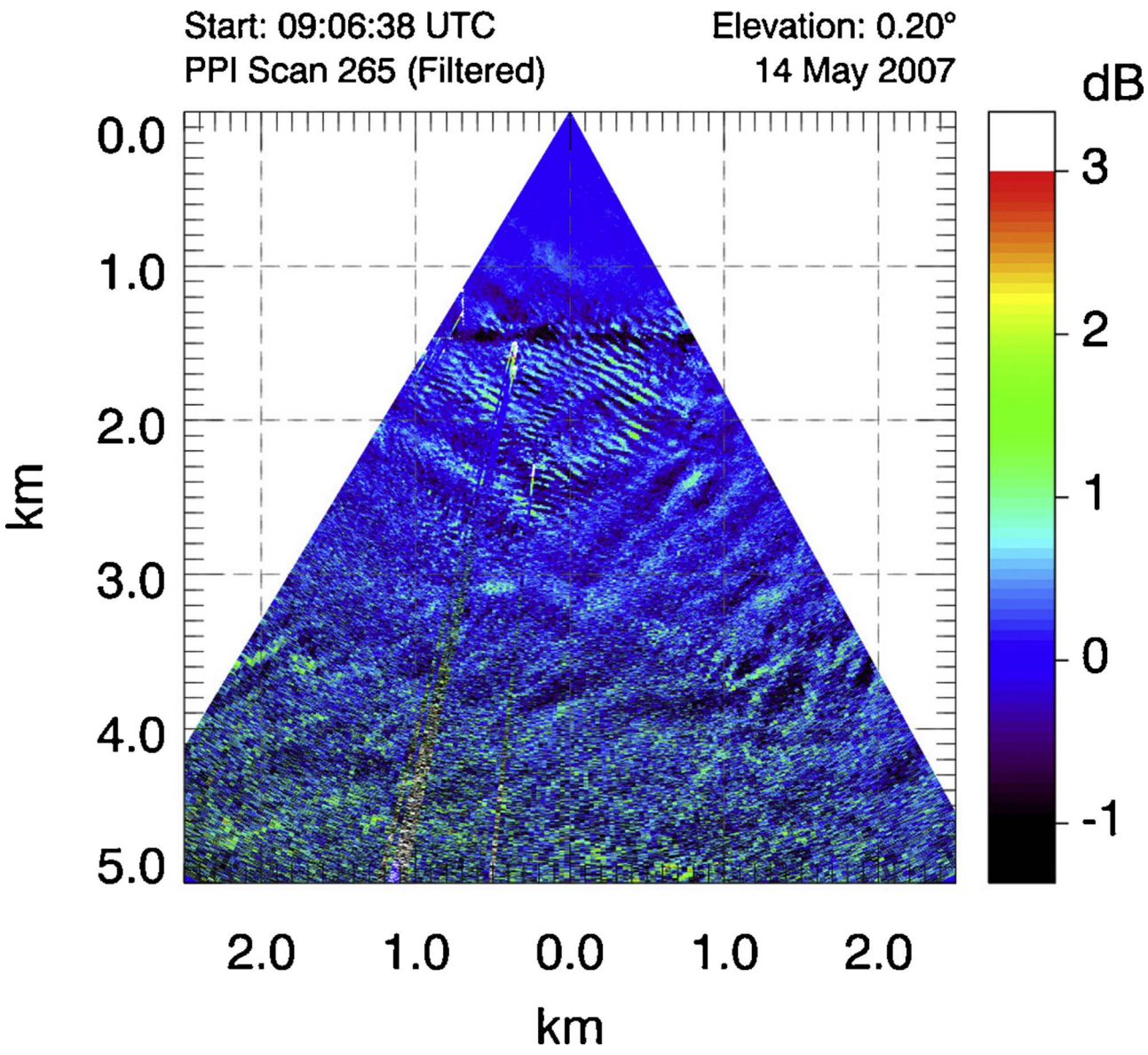

Fig. 3. High-pass median filtered elastic backscatter intensity from a single 60° wide PPI scan during wave episode number 34 on 14 May 2007 at 09:06 UTC. The scan took about 15 s to collect and is the result of about 150 laser pulses. (For interpretation of the references to color in this figure legend, the reader is referred to the web version of this article.)

square kilometer area of the lidar image surrounding the ISFF tower onto a dry erase board and tracing the wave crests manually with a pen. This resulted in a projected area of 56.5 cm × 56.5 cm. Therefore, a 100 m aerosol feature in the lidar image would appear as a 5.6 cm feature on the board and would be clearly identifiable. Because the waves were distributed across the area, and the wavelength often varied slightly in space, we strove to note the wavelength at wherever they were closest to the tower. In many cases clearly identifiable waves surrounded the tower, but in some cases it was easier to analyze the waves up to 100 or 200 m distance from the tower due to better coherence at that location. The orientation was determined by using a protractor and measuring the angle between true north and a wave crest in a clockwise fashion. For example, wave crests that ran from the northwest to the southeast (or vice versa) would correspond to 135°. East-west oriented waves correspond to 90°.

In addition to noting the wavelength and orientation, individual wave crests were tracked in order to determine the propagation velocity which is composed of a phase speed and phase propagation direction. In 13 of the 53 cases, it was not possible to obtain phase velocity due to the slow update rate of the PPI scans. For the other 40 cases, an attempt was made to track wave crests that passed through the ISFF tower location, but sometimes crests were tracked as far as a couple hundred meters away for clarity. It was possible in most cases to track a good wave crest over horizontal displacements of 100 m or more and spanning several frames over a couple minutes in time. The displacement of a crest divided by the time between frames provided the phase speed. The direction of the propagation was normal to the wave crest and recorded in the same fashion as wind direction: the direction from which the wave propagated. For example, a wave propagating from the southwest would have a 225° propagation direction. It is also possible to determine wavelength and propagation velocity objectively by applying algorithms to the lidar images. As shown by Randall (2015), an autocorrelation function of the filtered backscatter data in the vicinity of the tower can provide wavelength. A cross-correlation function computed from pairs of consecutive images can reveal the phase speed. The wave characteristics obtained from the lidar data and reported herein resulted from subjective analysis.

Next, wave period and wave amplitude were subjectively and objectively determined from the in situ data. Subjective determination was based on visual inspection of the time-series data and noting the

Table 1
All episodes of canopy waves observed during the 2007 CHATS experiment in Dixon, CA. Δt is the time between lidar scans. λ is the wavelength. **V** is the wave propagation velocity (speed and direction). P_l is the wave period deduced from the lidar data. P_w is the wave period observed in the sonic anemometer vertical velocity time series data. δw is vertical velocity amplitude. δT is the temperature amplitude. Γ_E is the environmental lapse rate. $\mathbf{V}_s$ is the environmental wind shear. Lapse rate and shear were based on in situ data taken at 9 m and 11 m AGL.

#	Date	Time range (UTC)	Lidar				In situ				
			Δt (s)	λ (m)	**V** (m s^{-1}, °)	P_l (s)	P_w (s)	δw (m s^{-1})	δT (°C)	Γ_E (K m^{-1})	$\mathbf{V}_s$ (m s^{-1})
1	19 March	12:25:25–12:28:17	17	60	1.1, 205	55	65	0.3	0.8	−0.03	0.21
2	21 March	06:52:45–06:57:56	17	60	1.2, 125	52	40	0.2	0.5	−0.01	0.17
3	21 March	07:06:41–07:11:24	17	50	1.1, 150	44	55	0.2	0.6	−0.02	0.20
4	23 March	05:22:39–05:29:34	17	75	0.5, 300	138	–	–	–	−0.21	0.29
5	24 March	05:44:40–05:49:17	17	80	1.4, 240	58	85	0.6	1.3	−0.00	0.21
6	26 March	10:01:43–10:04:18	17	60	1.5, 235	40	30	0.5	0.9	−0.10	0.22
7	30 March	06:45:10–06:52:29	17	50	0.9, 227	53	50	0.3	0.9	−0.05	0.18
8	06 April	12:59:18–13:01:36	17	40	0.9, 55	43	55	0.4	0.6	−0.06	0.18
9	19 April	05:40:21–05:55:35	27	40	1.1, 215	36	50	0.4	0.7	−0.19	0.24
10	19 April	06:13:40–06:17:38	17	45	1.4, 205	33	25	0.4	1.0	−0.11	0.37
11	24 April	13:00:22–13:02:11	11	30	0.7, 312	41	25	0.2	0.3	−0.23	0.15
12	24 April	13:11:01–13:24:21	11	50	1.1, 295	44	–	–	–	−0.02	0.17
13	25 April	10:17:23–10:27:58	30	50	–	–	40	0.4	0.8	−0.13	0.41
14	25 April	13:41:09–13:53:46	11	40	–	–	40	0.3	0.9	−0.09	0.23
15	26 April	07:01:32–07:24:14	30	35	–	–	45	0.2	0.6	−0.26	0.28
16	26 April	08:02:47–08:22:58	30	40	–	–	35	0.3	0.7	−0.08	0.24
17	26 April	08:39:06–08:56:45	30	40	–	–	–	–	–	−0.20	0.19
18	27 April	06:34:22–06:42:26	30	80	1.6, 227	49	45	0.5	1.0	−0.11	0.31
19	27 April	07:51:15–08:06:53	30	50	1.3, 215	40	30	0.4	1.4	−0.15	0.26
20	27 April	10:44:46–10:48:18	30	60	–	–	25	0.3	0.9	−0.14	0.30
21	27 April	12:47:37–12:50:39	30	50	0.8, 237	61	30	0.3	0.8	−0.18	0.12
22	27 April	13:51:54–14:05:01	30	35	–	–	35	0.3	0.8	−0.09	0.24
23	30 April	09:39:55–09:52:01	30	80	0.7, 205	110	30	0.2	–	−0.22	0.17
24	30 April	10:31:51–10:56:04	30	65	1.0, 185	66	40	0.3	0.8	−0.14	0.37
25	30 April	12:35:57–12:51:35	30	40	–	–	40	0.5	0.9	−0.01	0.27
26	05 May	05:23:17–05:47:07	17	100	2.0, 235	51	55	0.4	1.0	−0.06	0.32
27	08 May	08:04:25–08:09:28	30	60	1.3, 210	46	55	0.5	1.7	−0.13	0.39
28	11 May	10:03:32–10:10:05	30	90	1.3, 180	68	55	0.4	0.6	−0.13	0.36
29	11 May	11:08:49–11:13:21	30	40	–	–	60	0.4	0.5	−0.05	0.13
30	11 May	12:00:15–12:05:06	30	60	1.5, 380	40	55	0.3	0.7	−0.07	0.28
31	11 May	13:23:46–13:30:19	30	30	–	–	45	0.3	0.5	−0.18	0.15
32	11 May	13:43:10–13:49:13	30	30	–	–	40	0.3	0.5	−0.01	0.13
33	13 May	08:56:27–09:03:00	30	50	0.8, 310	60	65	0.3	–	−0.05	0.15
34	14 May	08:00:34–09:11:11	30	60	1.3, 215	45	35	0.5	2.0	−0.08	0.29
35	14 May	13:17:07–13:20:39	30	30	–	–	45	0.3	0.9	−0.20	0.22
36	24 May	11:38:40–11:43:56	11	95	1.7, 150	57	60	0.3	0.8	−0.21	0.28
37	25 May	10:50:31–10:57:03	11	30	0.9, 150	33	45	0.2	0.7	−0.14	0.25
38	26 May	12:55:15–13:09:24	17	55	1.0, 210	58	60	0.3	0.7	−0.02	0.20
39	28 May	13:24:22–13:40:12	17	45	0.6, 313	75	60	0.3	–	−0.06	0.11
40	02 June	10:33:34–10:39:44	11	60	1.0, 210	59	30	0.4	0.7	−0.03	0.24
41	03 June	09:49:28–09:52:44	11	30	0.9, 195	33	40	0.3	–	−0.02	0.23
42	03 June	13:23:51–13:26:09	17	55	0.5, 230	111	100	0.3	0.8	−0.01	0.14
43	08 June	09:11:15–09:14:47	30	60	1.3, 155	46	35	0.3	1.2	−0.11	0.33
44	08 June	11:25:12–11:42:04	30	70	1.7, 220	42	45	0.4	0.7	−0.06	0.24
45	08 June	11:54:10–12:01:44	30	80	1.4, 200	58	65	0.3	0.8	−0.13	0.23
46	08 June	13:05:19–13:15:24	30	60	1.1, 233	54	40	0.3	0.8	−0.07	0.24
47	08 June	13:17:55–13:24:28	30	80	1.3, 237	61	30	0.3	0.8	−0.05	0.23
48	09 June	10:06:18–10:20:25	30	60	1.0, 140	60	60	0.4	0.7	−0.15	0.35
49	09 June	10:39:35–11:12:24	30	70	1.1, 115	65	50	0.4	0.6	−0.01	0.17
50	09 June	13:10:12–13:18:47	30	40	0.9, 215	45	60	0.2	0.4	−0.31	0.23
51	10 June	10:50:06–11:21:50	11	50	1.0, 233	50	50	0.4	1.3	−0.05	0.29
52	11 June	09:41:55–10:37:07	30	40	1.0, 245	40	35	0.3	0.8	−0.12	0.21
53	31 March	07:31:00–07:39:00	–	–	–	–	–	0.4	2.2	−0.18	0.24

time between the most apparent crests and the maximum vertical velocity in those waves. Objective determination of the period was based on the calculation of power spectra. The average temperature and wind profile for the corresponding 5 min was also calculated. From these, buoyancy and wind shear were calculated. The gradient Richardson number, the ratio of static stability to vertical wind shear, was also calculated to determine if the shear was sufficiently large to overcome the stability and excite wave activity. Table 1 lists the dates, times, and main characteristics of the waves and their environments for all episodes.

6. Case studies

6.1. Episode 34: 14 May 2007

This episode is presented first because the waves may be the most pronounced of the 53 cases, especially in the in situ data. This case also had the longest duration at 1 h 11 min (08:00:34–09:11:11 UTC) corresponding to a period approximately 4–5 h after sunset. During this time the lidar was programmed to alternate between RHI and PPI scans and therefore the temporal resolution of the horizontal image sequence was poorer relative to some of the other cases. Like most of the other cases, the waves do not appear in the RHI scans because only two laser

pulses were projected at altitudes below the top of the tower.[5] PPI scans were repeated every 30.3 s. Each PPI scan covered 60° of azimuth at a recorded elevation angle of 0.20° (see Fig. 3.) A time-lapse animation of the PPI scans from this episode is available in Supplementary material.

Within the 1 h 11 min episode, a five minute period of time is focused upon when the waves were the most pronounced in the lidar and in situ data: 9:04 to 9:09 UTC. Fig. 4 shows a 1 km by 1 km subset of one scan centered on the ISFF tower at 9:06:38 UTC. In this image, approximately 15 parallel bands of enhanced backscatter with a wavelength of about 60 m can be identified. The lidar scan is estimated to be about 18 m AGL in the vicinity of the tower in this case. The waves in this episode were oriented toward 120° azimuth and they propagated from 210° azimuth. By tracking a wave crest for 80 m of displacement over 60 s of time, it was determined that the wave propagation speed was 1.3 m s^{-1}. The waves exist up to the edge of the forest canopy at about 1.4 km range from the lidar but do not appear to be present in the area absent of trees that is north and downstream of the orchard. The very bright streaks and shadows starting at about 1.5 km range on the left side of the image are the result of hard target reflections from a cluster of taller trees near a group of farm buildings. During this episode, the atmosphere between the top of the canopy (at 10 m AGL) and the top of the tower (at 29 m AGL) was statically stable with an average lapse rate of -0.275 K m^{-1} and a mean temperature of 15.4°C at 18 m, the estimated height of the lidar scan at the range of the tower. This lapse rate corresponds to a Brunt-Väisälä frequency of 0.097 Hz and a period of 10.3 s.

Oscillations are present in the in situ time series data (see Fig. 5) and appear to be quite vertically coherent from within the canopy (< 10 m) to the top of the tower (29 m). Fig. 5 also reveals that the oscillations have a decreasing amplitude with increasing distance from 18 m AGL suggesting they are evanescent. From the sonic anemometer data, the waves have a vertical velocity (w) amplitude[6] of approximately 0.5 m s^{-1} and a period of approximately 40 s. If the wave train is assumed to be sinusoidal in shape with a maximum vertical velocity of 0.50 m s^{-1}, integration of vertical velocity from 0 to 10 s (one quarter of a 40 s wave cycle) results in a positive vertical displacement of 3.2 m. Therefore, the altitude range of an otherwise horizontal atmospheric layer at 18 m AGL in this wave train would undulate between 14.8 and 21.3 m AGL. Time series data of temperature (T) also exhibit oscillations with a period of 40 s and an amplitude as much as 3°C at 18 m (see Fig. 6). These two variables (w and T) oscillated with a 90° phase difference and support the notion that, unlike turbulence, waves do not result in vertical temperature flux (Stull, 1988). However, there is no phase shift between vertical velocity and relative humidity oscillations (not shown) at 18 m that change by as much as 3.6% from maxima to minima with a mean of 65%.

The mean wind during this period was from the south at altitudes below the canopy and it increased in speed and veered from 10 m to 29 m AGL (see Fig. 7). Oscillations are present in the horizontal velocities in both speed and direction and a 90° phase shift is also apparent between vertical and horizontal wind speeds. Oscillations in both magnitude and direction are present at the same period as the oscillations in the vertical velocity and temperature. To identify the altitude of maximum wave amplitude, the standard deviation of vertical velocity was calculated at each height. The fluctuations due to wave motion are assumed to be the greatest contributor to the standard deviation and that contributions from turbulence are relatively small. Therefore, the height with the highest standard deviation is the height with the greatest wave amplitude. In this episode, that height is 18 m but the amplitude at the 14 m altitude is almost equal. Since 18 m is also the height that is closest to the lidar scan plane, it may explain why this case exhibits such intense crests of enhanced backscatter relative to some of the other cases.

[5] The RHI scans typically ranged from near 0° to 35° elevation.

[6] The amplitude is defined as the maximum deviation from the mean.

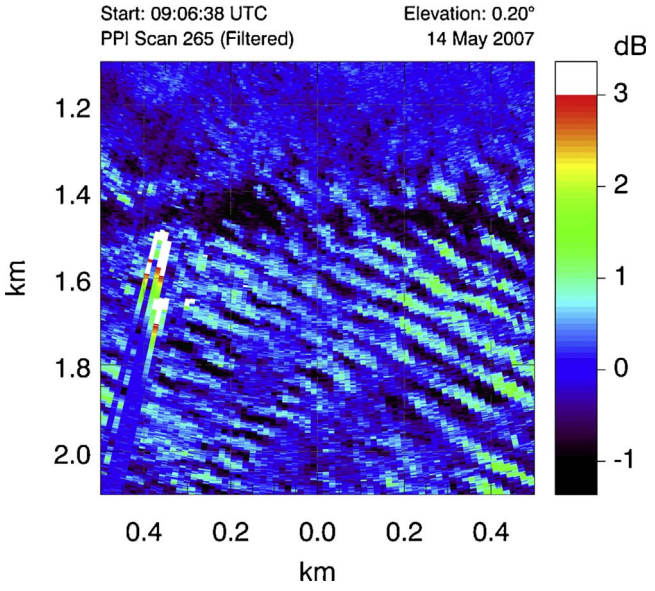

Fig. 4. High-pass median filtered elastic backscatter intensity from a single PPI scan over a 1 km^2 region surrounding the 30-m tower for the wave episode 34 on 14 May 2007 at 09:06 UTC. The region shown is indicated by a white square in Fig. 1. Sievers Road runs east-west at 1.45 km south of the REAL. The bright streaks on the left side of the image were caused by tall trees near a group of farm buildings. Approximately 15 wave crests (green bands) can be identified over the orchard. Each wave crest in this episode does not exhibit the asymmetry show in Fig. 2e. (For interpretation of the references to color in this figure legend, the reader is referred to the web version of this article.)

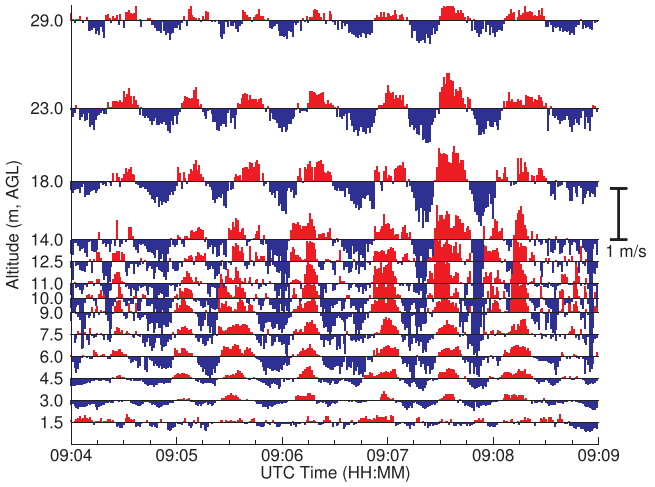

Fig. 5. Time series of vertical velocity from 13 tower-mounted sonic anemometers during wave episode 34 that occurred on 14 May. Data from each height is plotted simultaneously with the length of each bar indicating the magnitude of the vertical velocity. Upward motions are in red and downward are in blue for clarity. (For interpretation of the references to color in this figure legend, the reader is referred to the web version of this article.)

6.2. Episode 11: 24 April 2007

This episode was selected for exposition mainly because the waves had the shortest wavelength (30 m) of any in the 53 cases (5 of the 53 cases had this same short wavelength) and propagated from the northwest. This is noteworthy because flow from the NW experiences a relatively short fetch (about 70 m) over the canopy prior to reaching the tower and the PPI scans suggest that the waves form approximately within 50 m of the edge of the canopy. Wave crests begin to emerge in the lidar PPI scans between 12:58 and 12:59 UTC and are very pronounced in the last frame of this sequence at 13:02:11 UTC. During this time, the REAL was collecting narrow (10° in azimuthal range) PPI sector scans (as shown in Fig. 8) with an update every 11 s. Given the

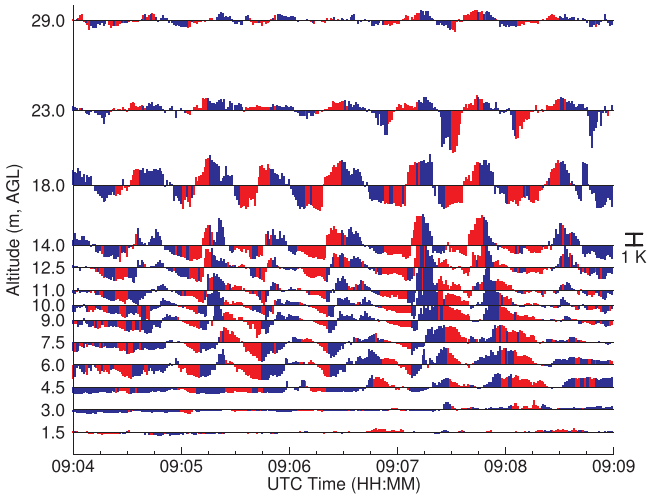

Fig. 6. Time series of air temperature from 13 tower-mounted sensors during wave episode 34 on 14 May 2007. Bars above each horizontal line indicate positive temperature perturbations and bars below the horizontal lines represent negative temperature perturbations. The bars are color coded according to the corresponding direction of vertical velocity shown in Fig. 5: red indicates upward motion and blue indicates downward motion. (For interpretation of the references to color in this figure legend, the reader is referred to the web version of this article.)

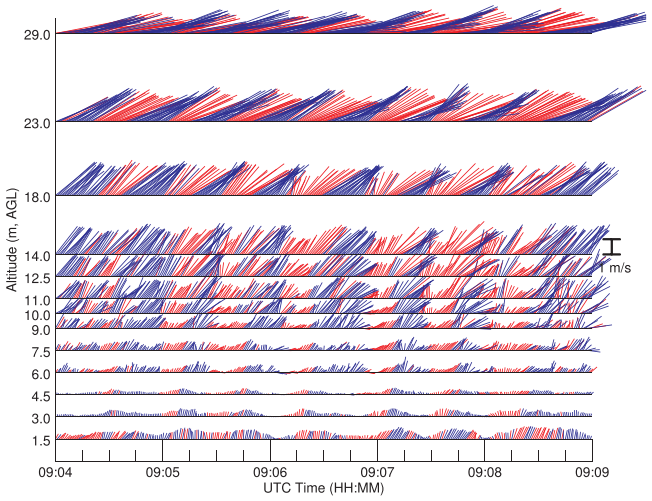

Fig. 7. Time series of horizontal wind vectors from sonic anemometer data for wave episode 34 on 14 May 2007. A vector pointing up would represent flow from the south. A vector pointing to the right would represent flow from the west. The vectors are color coded according to the corresponding direction of vertical velocity shown in Fig. 5: red indicates upward motion and blue indicates downward motion. (For interpretation of the references to color in this figure legend, the reader is referred to the web version of this article.)

laser pulse rate of 10 Hz, and the azimuthal scan rate of 0.925° s^{-1}, the distance between the lidar radial backscatter arrays at the range of the ISFF tower was about 2.6 m during this time—about 5 times more resolution in that dimension than the PPI data in the previous case. The presence of numerous hard targets shown in Fig. 8 indicates that the scan was lower in altitude than in many other episodes. For example, the white area in the upper left at about 1470 m south of the lidar was caused by the scan intersecting the east-west oriented power lines running along Sievers Road just north of the orchard. Random hard targets south of the power lines, mostly on the west side of the image are likely from the tops of orchard foliage. The short east-west oriented hard target at 1730 m range is the horizontal array structure. The 30 m tower was located directly in the center of the image at 1610 m range and a hard target reflection from it is also evident. A time-lapse animation of the PPI scans from this episode is available in Supplementary

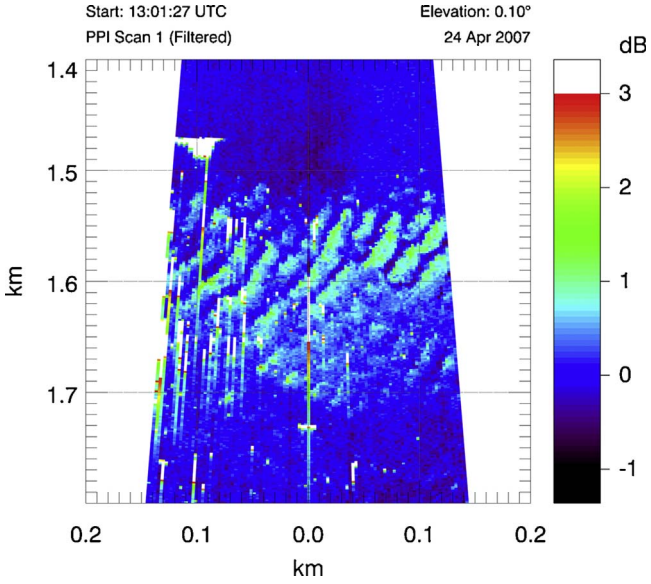

Fig. 8. High-pass median filtered elastic backscatter image over a 400 m × 400 m area centered on the ISFF tower for wave episode 11 on 24 April 2007 at 13:01 UTC. 6–8 wave crests (light blue to somewhat green ridges) are apparent at this time. The wind direction was from the northwest. The waves propagated from the northwest to the southeast. Some of the wave crests in this image exhibit the asymmetry shown in Fig. 2E. (For interpretation of the references to color in this figure legend, the reader is referred to the web version of this article.)

material. Oscillations in the vertical velocity traces from sonic anemometers (not shown) are not as coherent as in the previously presented case, and the data suggest that the variability may be more the result of turbulence, especially below 18 m AGL.

The set of narrow PPI scans as described above occurred as part of a repeating sequence of changing scan parameters that was executed to observe structure and motion on both nearly-horizontal and vertical cross-sections and over a range of spatial scales that is broader than what can be sampled by a REAL that is programmed to repeat one scan continuously. For example, it is very desirable to have both PPI scans to observe horizontal structure and RHI scans to observe vertical structure. It is also desirable to have narrow scans with high angular resolution and short update intervals that resolve fine-scale features and wide scans that provide a broader perspective of the region beyond the perimeter of the orchard. Therefore, the REAL was programmed to collect a repeating sequence of wide PPI, RHI, narrow PPI, RHI, etc., in an effort to satisfy all of these competing wishes. This episode is an example of when the narrow PPI scans revealed structure that would have been barely perceptible in the coarser wide PPI scans and it also showed the value of having RHI scans.

Just prior to the narrow PPI scans as shown in Fig. 8, the REAL was collecting RHI scans. After the identification of this episode in the PPI scans, the RHI scans were carefully examined for evidence of waves. Fig. 9 reveals periodic structures between approximately 30 and 50 m AGL. The structures, that resemble billows, are on a vertical gradient of aerosol backscatter and have a spacing, or wavelength, of about 100 m. It is interesting that they exist above the altitude of the PPI scan plane (that is closer to 10 m AGL in the narrow scans and 20 m AGL in the wide scans) and begin at 1.35 km range—north of the Sievers Road and the Cilker orchard and over short crops. It is also noteworthy that these waves tilt toward the south. Based on the wavelength, altitude, and location north of the road, it appears that the billows in the RHI scans are not a result of the orchard imparting an inflection point instability on the flow and are different from the waves in the PPI scans in Fig. 8. From 13:02 until 13:11, the lidar collected RHI scans again, but wave activity was not apparent at the canopy top, although there is evidence of billow-like structures north of the orchard at higher altitudes

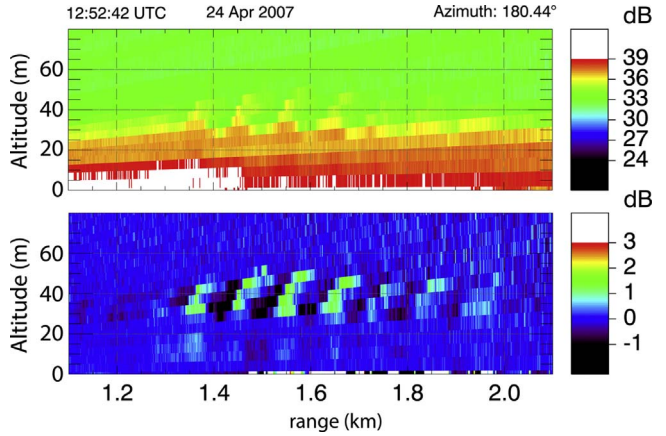

Fig. 9. One RHI scan at 12:52:42 just prior to episode 11 on 24 April 2007. The top panel shows range-corrected backscatter intensity without high-pass median filtering. The bottom panel shows the same data as the top panel, except with a 333-point (500 m) high-pass median filter applied in the radial dimension. (For interpretation of the references to color in this figure legend, the reader is referred to the web version of this article.)

(40–60 m AGL) and south of 2.25 km range between 20 and 40 m AGL. After 13:11, the lidar collected wide PPIs resulting in coarse resolution that made the waves more difficult to discern in the images.

6.3. Episode 36: 24 May 2007

This episode, with a duration of about 5 min 16 s, was chosen for exposition because the wavelength of the waves was among the longest of the 53 cases: about 95 m. The data analysis was focused on a 131 s period of time between 11:39:35 and 11:41:46 UTC. It appears the height of the PPI scan was close to the top of the canopy as numerous hard targets are apparent. In fact, hard target reflections are apparent from the power lines at 1.475 km range (western side of the sector scan) and there is also hard target evidence of the horizontal array structure at 1.73 km range. The lidar scan strategy was the same as in the previous case: narrow (10°) sector scans at an azimuthal scan rate of slightly less than $1^\circ\,s^{-1}$ (see Fig. 10). The wave crests were oriented toward 50°. The wind and the waves propagated from the SE to the NW at $1.7\ m\,s^{-1}$. Given the wavelength and phase speed obtained from the lidar data, the wave period should be about 57 s. Based on the lapse rate the Brunt-Väisälä period is about 15 s. Notice the sharper gradient in aerosol backscatter intensity on the upwind side of each wave crest. This characteristic was observed in 22 of the 53 episodes and it is hypothesized to result from the asymmetry of the waves when they begin to break with more laminar flow on the upwind side of each crest and turbulence occurring on the downstream side of each crest that results in diffusion of the aerosol backscatter gradient (see Section 4 and Fig. 2D and E). A time-lapse animation of the PPI scans from this episode is available in Supplementary material. Coherent oscillations in the in situ data at the altitude closest to the lidar scan are not as apparent. In fact, the vertical velocity trace at 14 m AGL (not shown) appears to be rather turbulent. However, there is evidence of waves with periods of approximately 1 min above this altitude and waves with periods of about 30 s below this altitude. The vertical velocity amplitude is about $0.5\ m\,s^{-1}$ and the amplitude of temperature perturbations is about 1.4°C.

6.4. Case 53: 31 March 2007

Unlike the others, this episode was discovered by careful inspection of the RHI scans long after the other 52 cases had been identified. Fig. 11 shows one RHI scan at 7:36:12 UTC that reveals at least 6 billows (perhaps as many as 9) in the bottom 30-m of the image. The peak altitude of the tallest billow in the series at this time is located at the

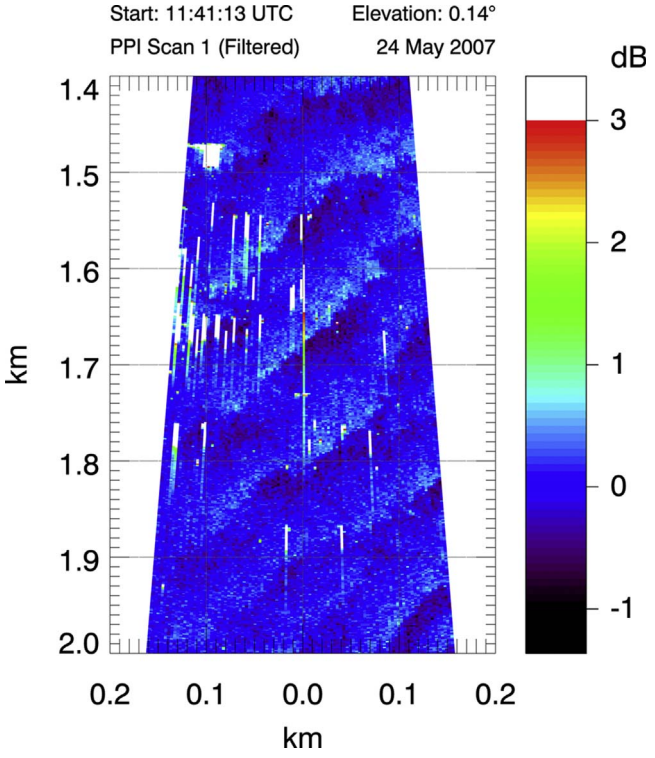

Fig. 10. A 400 m by 600 m area from a 10° wide PPI scan from episode 36 on 24 May 2007 at 11:41 UTC. The wind was from the SE during this episode and the wavelength was the longest at 95 m. The white pixels are the result of hard target returns. Notice the large gradient in backscatter intensity on the upwind side of each wave crest. The image reveals the asymmetry shown in Fig. 2e. (For interpretation of the references to color in this figure legend, the reader is referred to the web version of this article.)

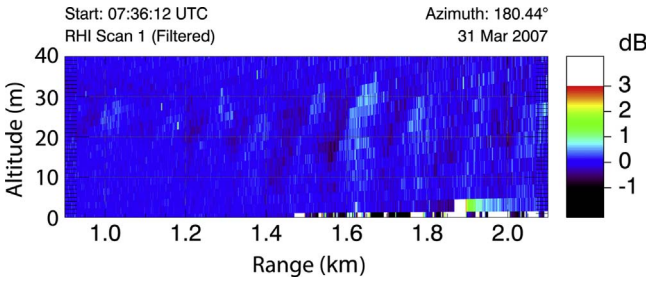

Fig. 11. One lidar RHI scan from episode 53 on 31 March 2007 at 07:36 UTC. The vertical altitude scale is expanded relative to the horizontal distance scale in order to see the features in this 40 m thick layer. The billows tilt downstream (to the right) and each billow presents a sharper gradient of aerosol backscatter on the upwind side. (For interpretation of the references to color in this figure legend, the reader is referred to the web version of this article.)

range of the ISFF tower (1.6 km) and is about 35 m. (Recall, the top ISFF anemometer was at 29 m AGL.) The billow structures are tilted toward the south (to the right in the image) with increasing altitude and show a larger gradient in backscatter intensity on the northern side of each billow. This is consistent with the asymmetric structure observed in the PPI scans in episode 36. These billows appear to be on the verge of breaking as high backscatter intensity pixels (light blue) are directly above low backscatter intensity pixels (purple). The spacing of the billows is approximately 100 m in the north-south direction of this scan. The PPI scans closest to this time (7:39:31 UTC) reveal very faint wave structures oriented 45° with wavelengths of approximately 100 to 150 m and propagating from the NW to the SE. This would be consistent with billows spaced between 70 and 105 m in the RHI scans. A time-lapse animation of the RHI scans from this episode is available in Supplementary material. Retrieval and plotting of the in situ data from near this time confirm the presence of waves that have a period of about

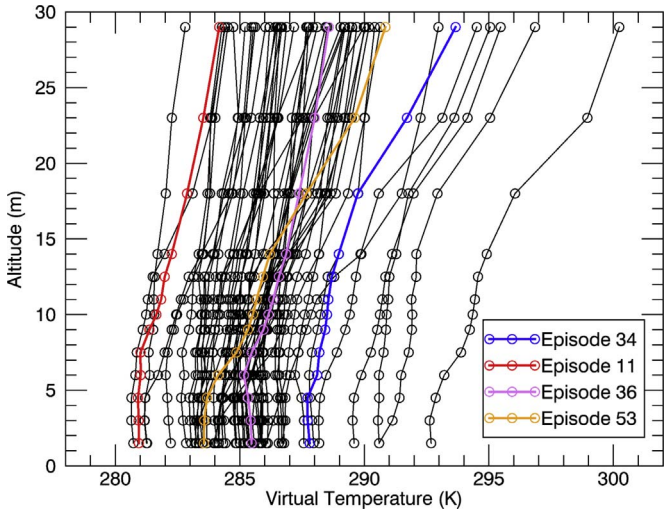

Fig. 12. Mean virtual temperature profiles for all episodes with the 4 described in Section 6 highlighted in color. (For interpretation of the references to color in this figure legend, the reader is referred to the web version of this article.)

135 s and a maximum vertical velocity amplitude of about 0.3 m s^{-1} at 7:36 UTC.

7. Summary of results from all cases

7.1. Environmental conditions

All of the wave episodes occurred during the night, when temperature inversions and relatively light winds were present. Figs. 12, 13, and 14 show the mean virtual temperature, relative humidity, and density profiles for all 53 episodes. Vertical profiles of mean horizontal wind speed, shear, and concavity for the 5-min focus periods in all 53 episodes are shown in Fig. 15. The overall mean wind speed profile (solid red line in the left panel of Fig. 15) has a minimum of 0.18 m s^{-1} at 4.5 m AGL and a maximum of 2.4 m s^{-1} at 29 m AGL. The maximum mean wind speed for any of the 53 cases is 4.16 m s^{-1}. The overall mean wind speed profile provides evidence that the canopy imparts drag on the mean flow and reduces the mean wind speed in the altitude range of the canopy. By taking the derivative of the wind speed profiles with respect to altitude, the wind shear was calculated. The middle panel in Fig. 15 shows the shear profiles for all 53 episodes and the overall mean shear profile (solid red line). A clear maximum in shear of 0.25 s^{-1} occurs at 10.5 m AGL which corresponds to the center of the

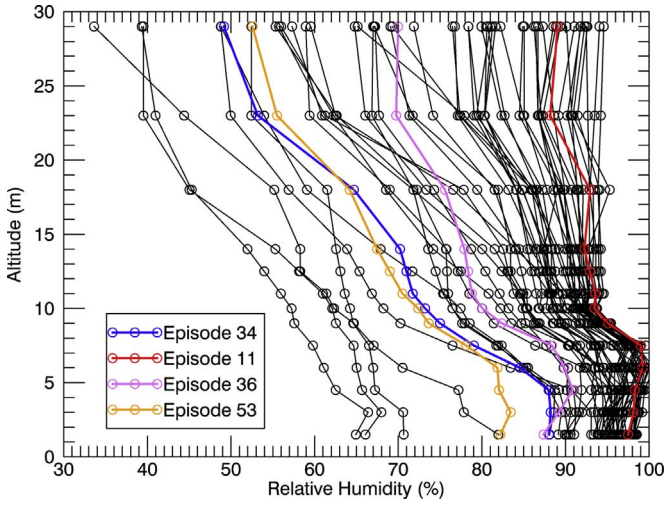

Fig. 13. Mean relative humidity profiles for all episodes.

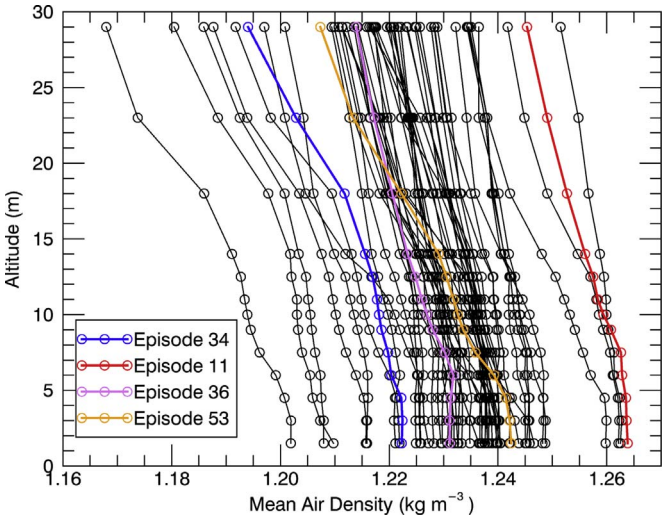

Fig. 14. Mean air density profiles for all episodes.

layer between the anemometers installed at 10 and 11 m AGL. Finally, the right panel in Fig. 15 quantifies what is visually apparent in the first panel: a change in the sign of concavity and the existence of an inflection point in the wind profiles. The values of concavity below 10 m AGL tend to be positive and the values of concavity above 10 m AGL tend to be negative. These data are consistent with the prevailing theory that the waves are generated by inflection point instability.

The thermodynamic and wind shear data are used to compute the gradient Richardson number (*Ri*) for each of the 53 episodes and are plotted in Fig. 16. The gradient Richardson number is defined as

$$\mathrm{Ri} = \frac{\frac{g}{T_v}\frac{\partial \Theta_v}{\partial z}}{\frac{\partial \overline{u}}{\partial z}^2 + \frac{\partial \overline{v}}{\partial z}^2} \quad (1)$$

where T_v is the virtual temperature, θ_v is the mean virtual potential temperature, and $\overline{u}$ and $\overline{v}$ are the mean wind components. In this work, mean thermodynamic and velocity data over the 5-min periods of time when the waves were most pronounced were used to calculate *Ri*. The partial derivatives in Eq. (1) were replaced with finite differences by using changes in measurements over corresponding distances between adjacent pairs of sensors on the ISFF tower. $\overline{T_v}$ was substituted for θ_v because the pressure changes between the sensor altitudes and the reference pressure of 1000 hPa in the equation for potential temperature were small (< 2%). The profiles of *Ri* for each episode show considerable scatter above and below the canopy height of 10 m, but are strongly clustered between 0 and 0.15 in the range of altitudes between 8 and 13 m AGL. This cluster of values at the canopy top is less than the critical Richardson number of 0.25 thereby indicating this region is dynamically unstable and prone to the generation of instability resulting in waves or turbulence. The *Ri* is notoriously noisy and may not be representative of the flow in certain situations (Grachev et al., 2012). For more on the subject of *Ri* as a function of scale, the reader is referred to Mahrt (2007), Balsley et al. (2008), Grachev et al. (2013), and Babić et al. (2016).

7.2. Wave characteristics

In an attempt to distinguish whether the waves are Kelvin-Helmholtz or Holmboe type, profiles of shear and buoyancy were calculated following several other investigations of shear-driven waves in stratified fluids (Smyth and Winters, 2003; Smyth, 2006, 2007).

$$b = -g\left(\frac{\rho - \rho_o}{\rho_o}\right) \quad (2)$$

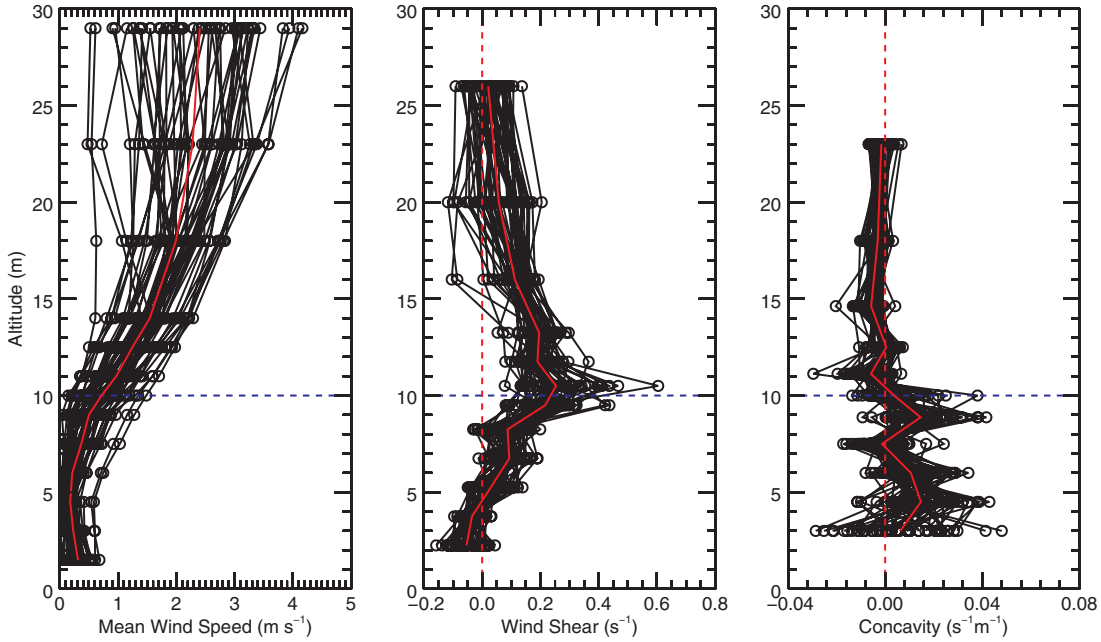

Fig. 15. Vertical profiles of mean horizontal wind speed (left), wind shear (middle), and concavity (right) for all episodes. The solid red line represents the mean of all episodes. The blue dashed line indicates the altitude of the top of the canopy. (For interpretation of the references to color in this figure legend, the reader is referred to the web version of this article.)

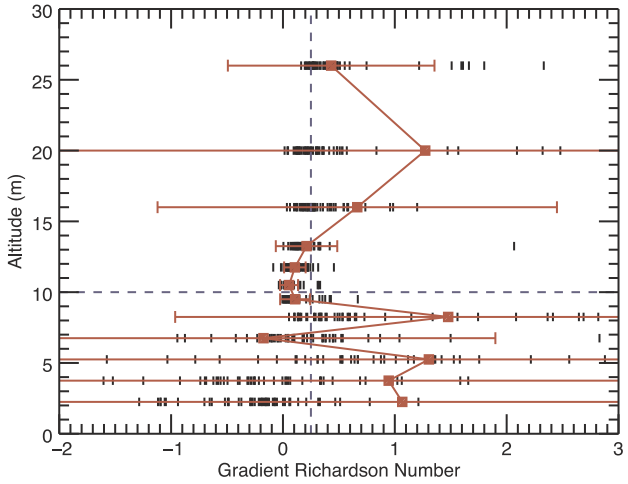

Fig. 16. Gradient Richardson number as a function of altitude for all the wave episodes. Black vertical lines as symbols represent the gradient Richardson numbers for each episode. Red squares represent the mean of all episodes at each level. Red error bars represent one standard deviation on each side of the mean. The vertical blue dashed line at 0.25 marks the critical Richardson number. The horizontal blue dashed line at 10 m AGL marks the canopy top. (For interpretation of the references to color in this figure legend, the reader is referred to the web version of this article.)

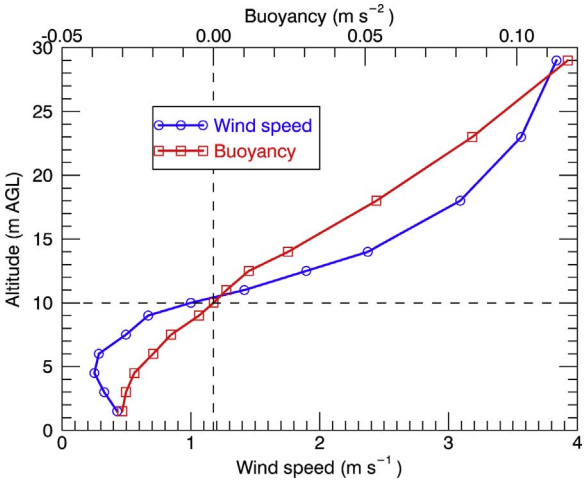

Fig. 17. Profiles of mean wind speed (blue) and buoyancy (red) as determined from the in situ data for all episodes. (For interpretation of the references to color in this figure legend, the reader is referred to the web version of this article.)

In Eq. (2), g is the acceleration due to gravity, ρ is air density, and ρ_0 is a characteristic density for each episode, set to the mean density at 10 m AGL. Appendix B describes how in situ observations from the ISFF tower sensors were used to calculate profiles of density and buoyancy. The mean buoyancy profile, relative to displacements from 10 m AGL, for all 53 episodes is shown in red in Fig. 17. Unlike two-layer fluid systems where the mean speed and density of each layer is clearly identifiable in vertical profiles, the mean wind speed and buoyancy profiles that support the canopy waves change continuously over the range of observed altitudes. It is not possible to identify two distinct layers of constant velocity and density with a transition zone in between over which buoyancy (or density) and velocity change. Therefore, this test is inconclusive in determining whether the waves are likely to be Kelvin-Helmholtz in nature rather than the Holmboe waves that arise when the buoyancy (or density) gradient is more compressed than the shear layer in two-layer fluids.

The most interesting quantitative result is that the waves propagate in the same direction as the wind but at phase speeds less than the mean wind speed (Figs. 18 and 19). This is based on following wave crests in the PPI scans and averaging the sonic anemometer velocity data at the altitude closest to the estimated altitude of the PPI scan at the range of the tower. Fig. 18 suggests that phase speed increases at about half the rate of the mean wind speed. The results are different from those published by Lee and Barr (1998) that show wave phase speed increasing proportionally with wind speed based on in situ data collected during BOREAS. In that study, wave phase velocity was calculated by applying a method described by Rees and Mobbs (1988) to data obtained from sensors on three towers spaced between 66 and 150 m from each other.

The wave period calculated from the lidar data and the period determined from the in situ data are not correlated. This is attributed to uncertainty in estimating wave period during such dynamic conditions. Both methods yield values ranging from 30 s to almost 2 min. But, on a

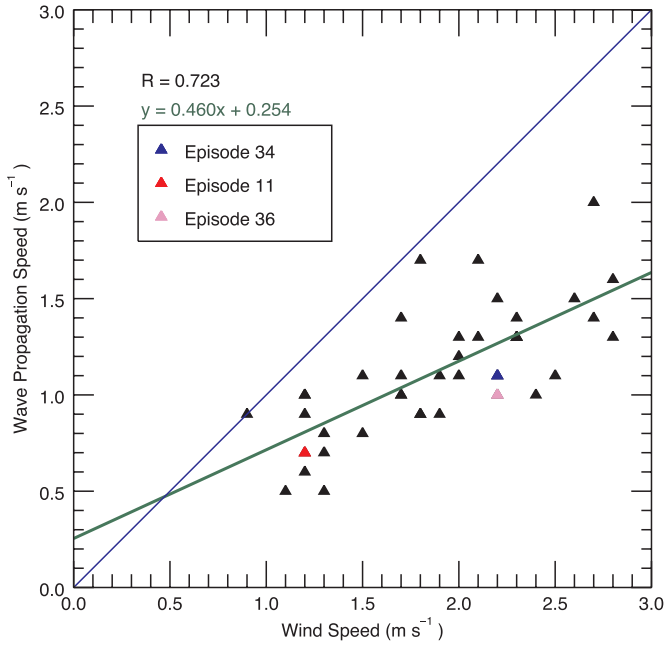

Fig. 18. Scatterplot of mean wind speed (from sonic anemometer data, at altitude of lidar scan) versus wave phase propagation speed (from lidar PPI scans) for the 40 episodes in which wave propagation velocity could be determined from the lidar data. Only 35 of 40 points plotted are apparent because 5 points are at the same location as others. The blue line is the identity line and the green line is the best-fit line. (For interpretation of the references to color in this figure legend, the reader is referred to the web version of this article.)

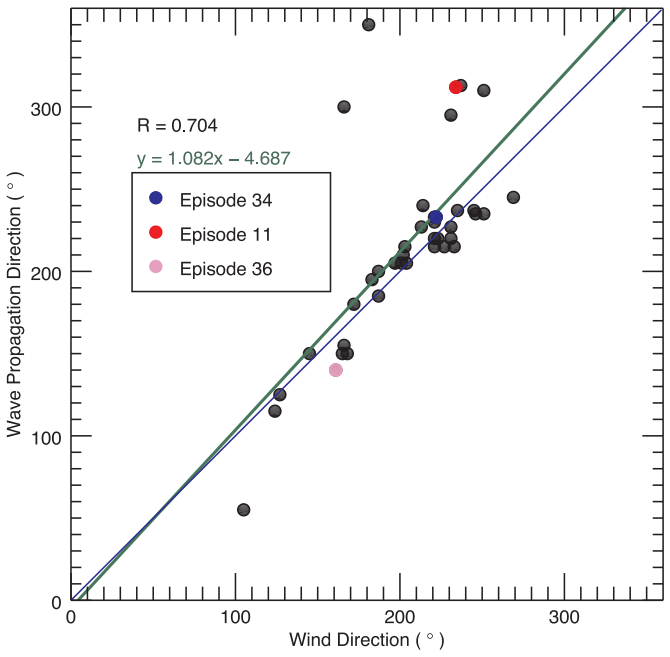

Fig. 19. Scatterplot of mean wind direction (from sonic anemometer data, at altitude of lidar scan) versus wave phase propagation direction (from lidar PPI scans) for the 40 episodes in which wave propagation velocity could be determined from the lidar data. The blue line is the identity line and the green line is the best-fit line. (For interpretation of the references to color in this figure legend, the reader is referred to the web version of this article.)

case-to-case basis, little to no correlation was found. The Brunt-Väisälä frequency and its reciprocal, the Brunt-Väisälä period, were calculated for each episode based on the mean lapse rate. The observed wave periods are consistently larger than the Brunt-Väisälä periods of which a majority ranged between 10 and 20 s. This is attributed to the fact that the canopy waves exist in an environment with wind shear which is not accounted for in measures of static stability such as the Brunt-Väisälä period.

Based on the experimental work by Held et al. (2012), changes in aerosol properties between the wave troughs and the crests can be estimated. The changes in observed aerosol scattering may be related to changes in particle concentration (associated with the vertical displacement of atmospheric layers) or to changes in the particle size distribution (as a result of changes in relative humidity as the air parcels ascend and decend), or both. Most of the episodes reveal a 1–2 dB change in backscatter intensity that corresponds to changes in concentration of 5–10 particles cm^{-3} (in the optical diameter range of 0.6–17 μm), or aerosol volume of 10–20 μm^{-3} cm^{-3}, or surface area of 8.5–17 μm^{2} cm^{-3}, or scattering coefficient of 20–40 m^{-1}. These values are found in Fig. 3 of the poster by Held et al. (2012).

In 22 of the 53 cases, asymmetry in the wave structure is apparent in the lidar data. That is, a sharper gradient of aerosol backscatter exists on the *upwind* side of the wave crest. The few RHI scans of waves that are available appear to show the wave crests tilted downwind with increasing altitude. This suggests that a majority of the cases (which do not show asymmetry in the PPI scans) are not close to breaking, but a significant number of cases are.

Perhaps the most intriguing aspect of the observations is the diversity of wavelengths (30–100 m) among all the episodes. Within a given episode, and at any given time, a small amount of spatial variability of wavelength may be noticed (for example, perhaps 10% or 20% of the mean wavelength). However, systematic changes in the wavelength in any given PPI scan were not apparent although a comprehensive analysis activity was not conducted to confirm this. In comparison, it has been suggested that canopy eddies during neutral conditions may grow in size and increase in spacing like those produced by a plane mixing layer (Raupach et al., 1996; Brown and Roshko, 1974). A spatial evolution of the wave characteristics across the orchard during these very stable conditions is not obvious in the lidar data. There is a strong correlation of waves over the canopy and not over the field without trees that is north of the orchard and Sievers Road. All of the wavelengths are longer than the altitudes at which they occur (< 29 m). Finally, temporal evolution of the waves is quite apparent: the lidar animations show that a field of waves may appear and disappear suddenly (within minutes). The episodes that form or dissipate quickly are likely to be related to sudden changes in the mean wind field and the concomitant changes in profiles of vertical shear. Such wind shifts are a documented feature of weak-wind nocturnal boundary layers (Mahrt, 2008, 2011) and they are also apparent in the time-lapse animations of REAL data from CHATS.

8. Conclusions

All of the evidence presented (with the exception of the lack of correlation in wave period deduced from the lidar data and the wave periods obtained through time-series analysis of in situ data) supports the hypothesis that the aerosol features observed in the lidar images are due to local microscale wave dynamics, and the in situ data support the hypothesis that the wave activity is due to inflection point instability generated by the presence of the canopy. Therefore, the lidar observations reveal the spatial structure and movement of canopy waves. This provides useful insights about the wavelength, the horizontal spatial extent of the waves, and the wave phase propagation velocity. The last sentence of Chimonas (2002) states: *Definitive investigations of boundary layer waves require technical advances to allow one to determine wave speeds within a fraction of a m s*$^{-1}$. That capability is now present considering that the position of a wave crest can be estimated to within about 10 m and at time intervals of about 20 s and greater. In future work, it would be interesting to compare the observed wavelengths and phase speeds with theory and numerical simulations that enable the modeling and prediction of those quantities.

In many of the cases, it was not possible to observe the wave phase speed due to the slow update rate of the PPI scans. Also, in many of the cases, the lidar did not observe the vertical structure of the waves due to the lack of vertical resolution in the RHI scans. However, RHI scans from one case did reveal waves and they resemble the structures routinely observed in other modeling studies and observations. For example, the structures in the lidar RHI scan image strongly resemble those in simulations (Klaassen and Peltier, 1985; Fritts et al., 1996; Gavrilov et al., 2011), and other observations such as Fig. 3c in van Haren and Gostiaux (2010) which are identified as Kelvin-Helmholtz billows observed near the bottom of the ocean.

The use of a scanning aerosol lidar to detect canopy waves is not necessarily surefire. For example, it is possible that the atmospheric volume in which the waves exist is filled with a uniform distribution of particulate matter in which case the waves would go undetected by the lidar. However, as described in Section 4, it is likely that vertical variations in aerosol optical scattering exist and that waves will appear in the imagery if the lidar is capable of detecting such small changes with high spatial and temporal resolution.

The relatively low altitude from which the laser pulses emanated from the REAL scanner during CHATS (about 3.8 m AGL) made it not possible to scan exactly horizontal over the orchard that was 10 m tall. The slightly inclined slope of the PPI scans prevented the instrument from sampling the atmosphere at altitudes near the canopy top at far ranges that corresponded to the southern border of the orchard and beyond. In future experiments, it would be useful to raise the lidar scanner to altitudes of about 10 m AGL or more in order to scan horizontally and observe the evolution of the waves across the entire orchard on a truly horizontal plane. After CHATS, the REAL was equipped with high precision sensors to record the pitch and roll of the instrument. In the future, the data from these sensors could be used in real-time to compensate for changes in the platform attitude and facilitate higher precision scanning.

Acknowledgments

This material is based upon work supported by the National Science Foundation's Physical and Dynamic Meteorology Program under award numbers AGS 0924407 and 1228464. Elizabeth Jachens, Tyson Randall, Chris Hasek, and Alexandra Smith supported the data analysis. Masaki Hamada and Annie Chen contributed Fig. 2. The author thanks Dr. Ned Patton, Dr. Jielun Sun, and the reviewers for helpful suggestions.

Appendix A. Calculation of laser beam bending

The vertical gradient of the refractive index of air was computed from

$$\frac{\mathrm{dn}}{\mathrm{dz}} = -\frac{n-1}{T}\left(\frac{\rho \mathrm{g\,T}}{P} - \gamma\right) \tag{A.1}$$

where n is the index of refraction of air, T is the air temperature, ρ is the air density, P is air pressure, and γ is the lapse rate (Mathscinotes, 2013). Alternative methods may be found in Doerry (2013). In this work, a value of 1.000274082 was used for the index of refraction of air at 1.543 μm wavelength (Ciddor, 1996). For the three deflections reported, the following conditions were used: air temperature of 285.8 K, air pressure of 100,900 Pa, and a density of 1.23 kg m^{-3}. The refraction radius was calculated from

$$r_R = \frac{n}{\frac{\mathrm{dn}}{\mathrm{dz}}}. \tag{A.2}$$

Appendix B. Calculation of thermodynamic quantities from ISFF data

This appendix describes how in situ measurements of temperature, surface pressure, and relative humidity from the ISFF were used to calculate mixing ratio, virtual temperature, pressure, and density as a function of altitude. Temperature and relative humidity measurements were made at 13 altitudes between 1.5 and 29.0 m AGL. Pressure measurements were made only at 1.0 m AGL. Therefore, as an initial condition, it was assumed that the pressure at 1.5 m AGL was the same as the pressure at 1.0 m AGL. For altitudes above 1.5 m AGL, the virtual temperature, pressure, and density, were estimated according to the following scheme.

First, mean temperature (T) and relative humidity (RH) were calculated from ISFF data for the 5-min focus periods of all 53 episodes. Saturation vapor pressure (e_s) was calculated in millibars following Bolton (1980):

$$e_s = 6.112 \exp\left(\frac{17.67T}{T + 243.5}\right) \tag{B.1}$$

where T is mean temperature in degrees Celsius. Saturation vapor pressure was then converted to Pascals ($e_s = 100e_s$) and vapor pressure (e) was calculated in Pascals from

$$e = e_s(0.\,01RH) \tag{B.2}$$

where RH is relative humidity as a percentage and 0.01 is a factor to change it into fractional form. Mixing ratio (r) was calculated using vapor pressure in Pascals, the ratio of the gas constants of dry air and water vapor estimated as 0.622, and actual pressure (p) in Pascals:

$$r = \frac{0.622e}{p - e}. \tag{B.3}$$

Temperature was converted from degrees Celsius to Kelvins. Then, virtual temperature (T_v) (see Fig. 12) was calculated in Kelvins using mixing ratio, actual temperature (T) in Kelvins, and the ratio of the gas constants of dry air and water vapor:

$$T_v = \frac{T\left(1 + \frac{r}{0.622}\right)}{1 + r}. \tag{B.4}$$

Pressures at altitudes above 1.5 m AGL were calculated using the hypsometric equation:

$$h = z_2 - z_1 = \frac{R_d T_v}{g} \ln\left(\frac{p_1}{p_2}\right) \tag{B.5}$$

where h is the thickness of the layer between altitudes z_1 and z_2 with corresponding pressures p_1 and p_2, $R_d = 287.04\ \mathrm{J\ kg^{-1}\ K^{-1}}$ is the dry air gas constant, and $g = 9.8\ \mathrm{m\ s^{-2}}$ is acceleration due to gravity. The hypsometric equation was rearranged to solve for p_2 at each subsequent altitude (z_2):

$$p_2 = \frac{p_1}{\exp\left[\frac{g(z_2 - z_1)}{R_d T_v}\right]}. \tag{B.6}$$

Finally, air density (ρ) (see Fig. 14) was calculated in $\mathrm{kg\ m^{-3}}$ using mean atmospheric pressure in Pascals, the dry air gas constant, and virtual temperature in Kelvins:

$$\rho = \frac{p}{R_d T_v}. \tag{B.7}$$

Appendix C. Supplementary data

Supplementary data associated with this article can be found, in the online version, at http://dx.doi.org/10.1016/j.agrformet.2017.05.014.

References

Arnqvist, J., Bergrström, H., Nappo, C., 2016. Examination of the mechanism behind observed canopy waves. Agric. For. Meteorol. 218–219, 196–203.

Babić, K., Rotach, M.W., Klaić, Z.B., 2016. Evaluation of local similarity theory in the wintertime nocturnal boundary layer over heterogeneous surface. Agric. For. Meteorol. 228–229, 164–179.

Bailey, B.B., Stoll, R., 2016. The creation and evolution of coherent structures in plant canopy flows and the role in turbulent transport. J. Fluid Mech. 789, 425–460.

Balsley, B.B., Svensson, G., Tjernström, M., 2008. On the scale-dependence of the gradient Richardson number in the residual layer. Bound. Layer Meteorol. 127 (1), 57–72.

Batchelor, G.K., 1967. An Introduction to Fluid Dynamics. Cambridge University Press.

Belcher, S.E., Harman, I.N., Finnigan, J.J., 2012. The wind in the willows: flows in forest canopies in complex terrain. Annu. Rev. Fluid Mech. 44, 479–504.

Bolton, D., 1980. The computation of equivalent potential temperature. Mon. Weather Rev. 108, 1046–1053.

Brown, G.L., Roshko, A., 1974. On density effects and large structure in turbulent mixing layers. J. Fluid Mech. 64 (4), 775–816.

Carpenter, J.R., Tedford, E.W., Heifetz, E., Lawrence, G.A., 2013. Instability in Stratified Shear Flow: Review of a Physical Interpretation Based on Interacting Waves. ASME. Appl. Mech Rev. 64 (6) 060801-060801-17.

Chimonas, G., 2002. On internal gravity waves associated with the stable boundary layer. Bound. Layer Meteorol. 102 (1), 139–155.

Ciddor, P.E., 1996. Refractive index of air: new equations for the visible and near infrared. Appl. Opt. 35 (9), 1566–1573.

Dérian, P., Mauzey, C.F., Mayor, S.D., 2015. Wavelet-based optical flow for two-component wind field estimation from single aerosol lidar data. J. Atmos. Ocean. Technol. 32, 1759–1778.

Doerry, A.W., 2013. Earth Curvature and Atmospheric Refraction Effects on Radar Signal Propagation. Tech. Rep. SAND2012-10690. Sandia National Laboratories 40 pp.

Dupont, S., Patton, E.G., 2012a. Influence of stability and seasonal canopy changes on micrometeorology within and above an orchard canopy: the CHATS experiment. Agric. For. Meteorol. 157, 11–29.

Dupont, S., Patton, E.G., 2012b. Momentum and scalar transport within a vegetation canopy following atmospheric stability and seasonal canopy changes: the chats experiment. Atmos. Chem. Phys. 12 (13), 5913–5935.

Fernando, H.J.S., Weil, J.C., 2010. Whither the stable boundary layer? Bull. Am. Meteorol. Soc. 91 (11), 1475–1484.

Finnigan, J.J., Shaw, R.H., Patton, E.G., 2009. Turbulence structure above a vegetation canopy. J. Fluid Mech. 637, 387–424.

Fitzjarrald, D.R., Moore, K.E., 1990. Mechanisms of nocturnal exchange between the rain forest and the atmosphere. J. Geophys. Res. 95 (D10), 16,839–16,850.

Fritts, D.C., Palmer, T.L., Andreassen, Ø., Lie, I., 1996. Evolution and breakdown of Kelvin-Helmholtz billows in stratified compressible flows. Part I: Comparison of two- and three-dimensional flows. J. Atmos. Sci. 53 (22), 3173–3191.

Gavrilov, K., Accary, G., Morvan, D., Lyubimov, D., Méradji, S., Bessonov, O., 2011. Numerical simulation of coherent structures over plant canopy. Flow Turbul. Combust. 86 (1), 89–111.

Grachev, A.A., Andreas, E.L., Fairall, C.W., Guest, P.S., Persson, P.O.G., 2012. Outlier problem in evaluating similarity functions in the stable atmospheric boundary layer. Bound.-Layer Meteorol. 144 (2), 137–155.

Grachev, A.A., Andreas, E.L., Fairall, C.W., Guest, P.S., Persson, P.O.G., 2013. The critical Richardson number and limits of applicability of local similarity theory in the stable boundary layer. Bound.-Layer Meteorol. 147 (1), 51–82.

Hamada, M., Dérian, P., Mauzey, C.F., Mayor, S.D., 2016. Optimization of the cross-correlation algorithm for two-component wind field estimation from single aerosol lidar data and comparison with Doppler lidar. J. Atmos. Ocean. Technol. 33, 81–101.

Held, A., Seith, T., Brooks, I.M., Norris, S.J., Mayor, S.D., 2012. Intercomparison of lidar aerosol backscatter and in-situ size distribution measurements. In: European Aerosol Conference. Granada, Spain, Presentation number B-WG01S2P05.

Hu, X., Lee, X., Stevens, D.E., Smith, R.B., 2002. A numerical study of nocturnal wavelike motion in forests. Bound.-Layer Meteorol. 102 (2), 199–223.

Jachens, E.R., Mayor, S.D., 2012. Lidar observations of fine-scale atmospheric gravity waves in the nocturnal boundary layer above an orchard canopy. In: 26th International Laser Radar Conference. Porto Heli, Greece.

Klaassen, G.P., Peltier, W.R., 1985. Evolution of finite amplitude Kelvin-Helmholtz billows in two spatial dimensions. J. Atmos. Sci. 42 (12), 1321–1339.

Kundu, P.K., Cohen, I.M., Dowling, D.R., 2016. Fluid Mechanics. Academic Press, Oxford, UK 921 pp.

Lawrence, G.A., Tedford, E.W., Carpenter, J.R., 2013. Instabilities in stratified shear flow. In: Venditti, J.G., Best, J.L., Church, M., Hardy, R.J. (Eds.), Coherent Flow Structures at Earth's Surface. John Wiley and Sons, Hoboken, pp. 63–71 (chap. 5).

Lee, X., 1997. Gravity waves in a forest: a linear analysis. J. Atmos. Sci. 54, 2574–2585.

Lee, X., Barr, A.G., 1998. Climatology of gravity waves in a forest. Q. J. R. Meterol. Soc. 124 (549), 1403–1419.

Lee, X., Black, T., den Hartog, G., Neumann, H.H., Nesic, Z., Olejnik, J., 1996. Carbon dioxide exchange and nocturnal processes over a mixed deciduous forest. Agric. For. Meterol. 81 (1–2), 13–29.

Lee, X., Neumann, H.H., Hartog, G.D., Fuentes, J.D., Black, T.A., Mickle, R.E., Yang, P.C., Blanken, P.D., 1997. Observation of gravity waves in a boreal forest. Bound. Layer Meteorol. 84, 383–398.

Mahrt, L., 2007. The influence of nonstationarity on the turbulent flux-gradient relationship for stable stratification. Bound.-Layer Meteorol. 125 (2), 245–264.

Mahrt, L., 2008. Mesoscale wind direction shifts in the stable boundary-layer. Tellus A 60 (4), 700–705.

Mahrt, L., 2011. Surface wind direction variability. J. Appl. Meteorol. Climatol. 50 (1), 144–152.

Mahrt, L., 2014. Stably stratified atmospheric boundary layers. Annu. Rev. Fluid Mech. 46 (1), 23–45.

Mathscinotes, 2013. Math Encounters Blog: Distance to the Horizon Assuming Refraction. wordpress.org (accessed 01.12.16). http://mathscinotes.com/2013/08/distance-to-the-horizon-assuming-refraction/.

Mayor, S.D., Dérian, P., Mauzey, C.F., Spuler, S.M., Ponsardin, P., Pruitt, J., Ramsey, D., Higdon, N.S., 2016. Comparison of an analog direct detection and a micropulse aerosol lidar at 1.5-micron wavelength for wind field observations–with first results over the ocean. J. Appl. Remote Sens. 10, 016031.

Mayor, S.D., Lowe, J.P., Mauzey, C.F., 2012. Two-component horizontal aerosol motion vectors in the atmospheric surface layer from a cross-correlation algorithm applied to scanning elastic backscatter lidar data. J. Atmos. Ocean. Technol. 29, 1585–1602.

Mayor, S.D., Spuler, S.M., 2004. Raman-shifted Eye-safe Aerosol Lidar. Appl. Opt. 43, 3915–3924.

Mayor, S.D., Spuler, S.M., Morley, B.M., Loew, E., 2007. Polarization lidar at 1.54-microns and observations of plumes from aerosol generators. Opt. Eng. 46 (9), 096201.

Nappo, C.J., 2012. An Introduction to Atmospheric Gravity Waves. Academic Press, Oxford, UK 400 pp.

Pahlow, M., Coauthors, 2006. Comparison between lidar and nephelometer measurements of aerosol hygroscopicity at the southern great plains atmospheric radiation measurement site. J. Geophys. Res.: Atmos. 111 (D5), d05S15.

Patton, E.G., Finnigan, J.J., 2013. Canopy turbulence. In: Fernando, H.J.S. (Ed.), Handbook of Environmental Fluid Dynamics, vol. 1. CRC Press/Taylor and Francis Group, LLC., pp. 311–327 (chap. 24).

Patton, E.G., Coauthors, 2011. The Canopy Horizontal Array Turbulence Study (CHATS). Bull. Am. Meteorol. Soc. 92, 593–611.

Paw U, K.T., Brunet, Y., Collineau, S., Shaw, R.H., Maitani, T., Qiu, J., Hipps, L., 1992. On coherent structures in turbulence above and within agricultural plant canopies. Agric. For. Meterol. 61 (1–2), 55–68.

Pulido, M., Chimonas, G., 2001. Forest canopy waves: the long-wavelength component. Bound. Layer Meteorol. 100, 209–224.

Randall, T.N., 2015. Observations of microscale gravity waves in the nocturnal boundary layer above an orchard canopy by a horizontally scanning lidar. Geological and Environmental Sciences, California State University Chico (M.S. thesis).

Raupach, M.R., Finnigan, J.J., Brunet, Y., 1996. Coherent eddies and turbulence in vegetation canopies: the mixing-layer analogy. Bound. Layer Meteorol. 78, 351–382.
Rees, J.M., Mobbs, S.D., 1988. Studies of internal gravity waves at Halley Base, Antarctica, using wind observations. Q. J. R. Meterol. Soc. 114 (482), 939–966.
Scorer, R.S., 1997. Dynamics of Meteorology and Climate. Praxis Publishing Ltd., West Sussex, England 686 pp.
Shaw, R.H., Patton, E.G., Finnigan, J.J., 2013. Coherent eddy structures over plant canopies. In: Venditti, J.G., Best, J.L., Church, M., Hardy, R.J. (Eds.), Coherent Flow Structures at Earth's Surface. John Wiley and Sons, Hoboken, pp. 149–159 (chap. 10).
Smyth, W.D., 2006. Secondary circulations in Holmboe waves. Phys. Fluids 18 (6), 064104.
Smyth, W.D., 2007. Mixing in symmetric Holmboe waves. J. Phys. Oceanogr. 37 (6), 1566–1583.
Smyth, W.D., Winters, K.B., 2003. Turbulence and mixing in Holmboe waves. J. Phys. Oceanogr. 33 (4), 694–711.
Spinhirne, J.D., 1993. Micro pulse lidar. IEEE Trans. Geosci. Remote Sens. 31, 48–55.
Spuler, S.M., Mayor, S.D., 2005. Scanning eye-safe elastic backscatter lidar at 1.54 microns. J. Atmos. Ocean. Technol. 22, 696–703.
Stull, R.B., 1988. An Introduction to Boundary Layer Meteorology. Kluwer, Boston.
Sun, J., Coauthors, 2015. Review of wave-turbulence interactions in the stable atmospheric boundary layer. Rev. Geophys. 53 (3), 956–993 2015RG000487.
Sutherland, B.R., 2010. Internal Gravity Waves. Cambridge University Press, Cambridge, UK 394 pp.
Thorpe, S.A., 2002. The axial coherence of Kelvin-Helmholtz billows. Q. J. R. Meterol. Soc. 128 (583), 1529–1542.
van Haren, H., Gostiaux, L., 2010. A deep-ocean Kelvin-Helmholtz billow train. Geophys. Res. Lett. 37 (3), l03605.